Paramagnetic borotungstate glasses with high terbium concentration for magneto-optical applications

Leonardo Vieira Albino, Marc Dussauze, Olivier Toulemonde, Mathieu Duttine, Veronique Jubera, Douglas Faza Franco, Thierry Cardinal, Marcelo Nalin

Journal of Non-Crystalline Solids XXX (XXXX) XXXXXX

Contents lists available at ScienceDirect

Journal of Non-Crystalline Solids

journal homepage: www.elsevier.com/locate/jnoncrysol

Paramagnetic borotungstate glasses with high terbium concentration for magneto-optical applications

Leonardo Vieira Albino [a,b,c,*], Marc Dussauze [c], Olivier Toulemonde [b], Mathieu Duttine [b], Véronique Jubera [b], Douglas Faza Franco [a], Thierry Cardinal [b,*], Marcelo Nalin [a,*]

[a] Laboratório de Vidros Especiais (LaViE), Institute of Chemistry, São Paulo State University (UNESP), Araraquara SP Brazil
[b] Univ. Bordeaux, CNRS, Bordeaux INP, ICMCB, UMR 5026, Pessac, F-33600, France
[c] Univ. Bordeaux, CNRS, ISM, UMR 5255, 33405 Talence, France

ARTICLE INFO

Keywords:
Borotungstate glasses
Magneto-optical glasses
Faraday rotators
Photonic glasses

ABSTRACT

Glass system xTb_2O_3-40WO_3-(60-x)B_2O_3, with x = 20; 22.5; 25 and 27.5 mol% were prepared by melting-quenching method. The samples were cut, polished and characterized by thermal, structural, optical, luminescent, magnetic and magneto-optical techniques aiming at applications in optical and magneto-optical devices. All terbium-containing samples exhibit magnetic response to neodymium magnets at room temperature. In addition, they feature thermal stability above 100 °C, wide transparency in the visible and near infrared region. Magnetic susceptibility measurements revealed the paramagnetic character of the terbium, with high Curie constants and antiparallel spin alignment. An ascending pattern in the Verdet constant was discerned as the concentration of Tb_2O_3 increased, culminating in a measurement of -124 rad·T^{-1}·m^{-1} at 632.8 nm for the sample containing 27.5 mol% Tb_2O_3. This value closely approximates those observed in terbium-borogermanates glasses and single-crystal TGG, representing an alternative for the development of novel, cost-effective magneto-optical vitreous materials.

1. Introduction

Nowadays, transparent glasses with magneto-optical (MO) properties are of great technological interest, due to the wide range of possibilities of applications including modulators, magneto-optical isolators, information storage devices, spintronic, magnetic and current sensors and magneto-optical glasses and fibers [1–8].

The magneto-optical effects are more pronounced in crystals containing a high concentration of ions with high paramagnetic susceptibilities, such as Fe^{3+} and, among the lanthanides, the trivalent terbium ion (Tb^{3+}) has electronic configuration $4f^8 \rightarrow 4f^7 5d^1$, with total angular momentum, $J = 6$, which promotes one of the highest values of total magnetic moment, being commercially applied in monocrystalline Faraday rotators such as yttrium iron garnet (YIG, +232 rad.T^{-1}.m^{-1} at 1.86 μm), terbium gallium garnet (TGG, −134 rad.T^{-1}.m^{-1} at 632.8 nm) and terbium aluminum garnet (TAG, −174 rad.T^{-1}.m^{-1} at 632.8 nm) [9–12]. However, the difficulty of synthesizing and modeling single crystals with dimensions greater than 10 cm limits their use in photonic devices, in addition to glasses with a high concentration of iron, generally, they can only be used as Faraday rotators in the infrared region, due to the high absorptions in the visible region. Thus, the development of new glass compositions containing a high concentration of Tb^{3+} ions has become an interesting alternative, with magneto-optical glasses exhibiting Verdet constants in the same magnitude as monocrystalline MO materials.

Several glass systems have high solubility for lanthanides, such as germanates[13], borates[14,15], borogermanates [1,2,16], gallogermanates [17], boro- and alumino-silicates [18–21] as well as phosphates [22–24]. The search for better and more efficient MO glass systems must ally four basic properties: high paramagnetic ions concentration, high refractive index, low absorption coefficient (in the operational spectral region) and high thermal stability against devitrification, to obtain large bulk samples and eventually optical fibers. Borotungstates [25–32], fulfil these requirements, presenting high solubility of Ln_2O_3, high refractive index (1.8–1.9) due to the higher polarizability of tungsten atoms, besides to be transparent from the visible to near infrared, include the telecom region (1.55 μm).

This work consisted of the synthesis and characterization of the

* Corresponding authors.
E-mail addresses: leonardoalbino63@gmail.com (L.V. Albino), thierry.cardinal@icmcb.cnrs.fr (T. Cardinal), marcelo.nalin@unesp.br (M. Nalin).

glassy system based on xTb_2O_3–$40WO_3$-$(60-x)B_2O_3$ (where $15 \geq x \geq 30$ mol%). The samples were obtained by melt-quenching and characterized by means of thermal analysis, X-ray diffraction, Raman scattering, FTIR, UV–Vis, fluorescence spectroscopies and magnetic and magneto-optical analysis. In order to access additional structural information, especially about the local environment of boron using ^{11}B Solid-State NMR, paramagnetic terbium ions have been replace for diamagnetic lanthanum cations.

2. Materials and methods

2.1. Synthesis of samples

Samples were prepared by the traditional melt-quenching technique, using chemical-grade tungsten oxide (WO_3, 99.8 % AlfaAesar), boric acid (H_3BO_3, 99.9995 % AlfaAesar Puratronic) and terbium oxide (Tb_2O_3, 99.99% Fox-Chemicals GmbH). To obtain vitreous boron oxide, thermal dehydration of boric acid was performed at 500 °C for 30 min in an electric furnace.

Then, the other compounds, previously homogenized, were placed into the Pt crucible together with B_2O_3 and melted in an electric furnace at 1250 °C for 1 h. After that, the furnace temperature is raised to 1350 °C for 10 min, aiming to reduce the viscosity of the molten glass. The glasses were formed by quenching the liquid into a steel mold kept at 590 °C and left at this temperature for 4 h for annealing before being slowly cooled down (1 °C . min^{-1}) to room temperature to reduce residual mechanical stress.

2.2. Characterization

Characteristic temperatures were measured by differential scanning calorimetry using the Netzsch DSC Pegasus 404 PC equipment, using small glass pieces (few mg) in a Pt pan at a heating rate of 10 °C/min up to 900 °C with a precision of ± 3 °C for glass transition (Tg) and onset of crystallization (Tx).

The vitreous state of the samples studied was evaluated by X-Ray diffraction analysis (XRD) collected on a PANalitycal X′pert PRO MPD diffractometer in Bragg−Brentano θ−θ geometry, equipped with a secondary monochromator and X′Celerator multi-strip detector. Each measurement was made within an angular range of $2\theta = 8 - 80°$. The Cu Kα radiation was generated at 45 kV and 40 mA ($\lambda = 0.15418$ nm).

The densities, ρ, were obtained by the Archimedes method, by immersing the samples in diethylphthalate at room temperature, measured by a mercury thermometer, on a Precisa XT 220A analytical balance (error of ± 0.0001 g). Each sample was measured five times, immersing and cleaning it properly after each immersion. Later, the mean and the standard deviation were calculated for each sample (± 0.0005 g).

Raman spectra were recorded from 200 to 2000 cm^{-1} with a confocal micro-Raman spectrometer LabRAM HR Evolution (Horiba Jobin Yvon) equipped with a Synapse CCD detector using a 532 nm radiation from a diode pumped solid state laser (output power = 20 mW) using a microscope with a 50x objective (NA = 0.27, Olympus).

Fourier-transform infrared spectroscopy (FTIR) analyzes carried out in the NICOLET IS5 equipment, Transmission module iD1 Transmission - Thermo Scientific. 4000–400 cm^{-1} scan, 64 scan background, 64 scan sample analysis, 2 cm-1 resolution. Samples were diluted in KBr for Merck spectroscopy and pressed in a pastillator for 1 min, under a pressure of 5 tons.

^{11}B Solid-State Nuclear Magnetic Resonance (NMR) were performed under Magic Angle Spinning (MAS) conditions (MAS rate 30 kHz) with a Bruker Avance III 500WB spectrometer (B_0=11.7 T) equipped with a MAS BL2.5 DVT X-1H probe. ^{11}B MAS NMR spectra were recorded using a single short-pulse sequence with a π/8 pulse length of 1 μs and an optimal recycle delay ranging from 5 to 50 s depending on the analyzed sample. Solid KBF_4 ($\delta_{iso}[^{11}B]$=0.50 ppm) was used as secondary reference compound to calibrate the ^{11}B NMR shift scale.

Transmission spectra in the Ultraviolet–visible–near infrared spectrometry and in the IR ranges were obtained using an Agilent Cary 5000 (UV–Visible-NIR) and Bruker Equinox 55 (FTIR) spectrometers, respectively.

Photoluminescence measurements were made at room temperature using a Horiba Jobin Yvon Spectrofluorimeter, Model Fluorolog-3 FL3–122.

Magnetic susceptibility was collected using a Quantum Design MPMSXL magnetometer in the temperature range of 5–150 K under 100 Oe (= 0.0001 T) in a zero-field cooling mode (ZFC). Field cooling results presented the same behavior.

The Faraday effect was measured at room temperature using a home-made optical setup. A 632.8 nm He-Ne laser beam passes through a polarizer and then through a solenoid with a tunable magnetic field up to 0.13 T. The beam then passes through another polarizer, rotated from 90° before reaching the photodetector. The errors associated to measurement of the rotation angle of the laser is 1°. The length of the samples were ~20 mm, corresponding to the optical path. The glasses were put into the solenoid and the first measurement was done without magnetic field. Then, after apply the magnetic field, the second polarizer is rotated to reset the maximum signal at the photodetector. This procedure was reproduced five times for each sample and the values recorded were used to obtain the average. As V is temperature dependent, the measurements were all taken at 22 °C. The magnetic field was calibrated using a gaussmeter and confirmed by measuring of the commercial TGG single crystal (−134 rad.T^{-1}.m^{-1}).

3. Results and discussions

Fig. 1 presents the ternary diagram for Tb_2O_3-WO_3-B_2O_3 ternary system studied, with the green spheres indicating the glassy samples and the red squares the samples that crystallized already in the pouring, showing that the system presents a reduced glass-forming region. We will focus on the series of samples xTb_2O_3-$40WO_3$-$(60-x)B_2O_3$ in which it was possible to produce glassy materials with high concentration of Tb_2O_3 and WO_3 without detecting crystallization. The high concentration of WO_3 increases the density and refractive index of the samples, and the Tb_2O_3 contains the paramagnetic ion of interest, all desirable characteristics for Faraday rotators [34].

Batches of 7.0 g of xTb_2O_3–$40WO_3$-$(60-x)B_2O_3$, $x = 15$, 20, 22.5, 25, 27.5, 30, samples were prepared by the traditional melt-quenching technique, as specified. Samples with 20, 22.5, 25 and 27.5 mol% Tb_2O_3 presented a very glassy and homogeneous appearance, however the samples containing 15 and 30 mol% Tb_2O_3 presented signs of crystallization after quenching, showing how the glass-forming region in

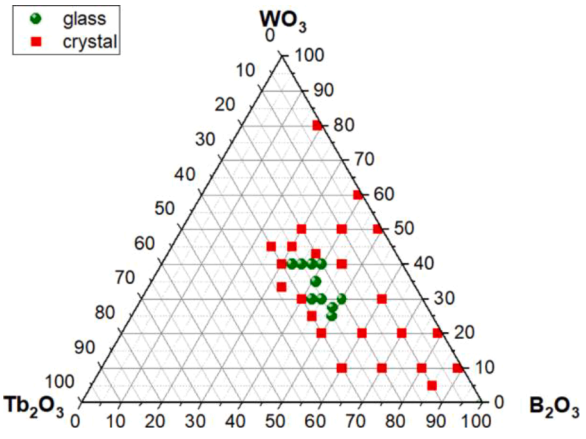

Fig. 1. Ternary diagram of compositions in the Tb_2O_3-WO_3-B_2O_3 system. Green spheres correspond to glass samples and red square to crystallized compositions.

this condition is limited.

The glassy samples were cut and polished for further optical characterizations, as seen in Fig. 2a. All samples show magnetic behavior, being attracted by commercial neodymium magnets (N52) at room temperature (Fig. 2b). The acronyms, nominal compositions, in mol% and cationic percent of investigated samples are summarized in Table 1.

3.1. XRD, thermal analysis, density and optical basicity

The formation of vitreous phases was verified by XRD and thermal analysis as shown in Figs. 3 and 4a., respectively [35,36]. Lines for determining characteristic temperatures have been drawn as eye guides to facilitate understanding in Fig. 4a. The diffractograms reveal the presence of crystalline phases for samples 15Tb40W and 30Tb40W, indicating a low stability against devitrification for such compositions. The high concentration of Tb_2O_3 (> 27.5% mol) favors the precipitation of a $TbBO_3$ hexagonal phase group P63/mmc, JCPDS file number (01-074-1933) which corresponds to $DyBO_3$, showed in Fig. 3. For 15Tb40W we have identified triclinic phase group P-1, $Tb_{11}O_{20}$ (03-065-3996). For concentrations below 15 mol%, polycrystalline precipitation occurs, characteristic of rare earth borates [37]. On the other hand, samples 20Tb40W, 22.5Tb40W, 25Tb40W and 27.5Tb40W did not present such peaks and exhibit the diffraction halos characteristic of glassy materials.

Fig. 4b shows the glass transition temperature (Tg) and thermal stability parameter, ΔT (ΔT = Tx-Tg), variation, with lines drawn connecting specific points to facilitate understanding. From Tg variation, that increases as a function of the content of terbium, passing from 589 to 648 °C for samples containing 20 and 27.5 mol% of Tb_2O_3, respectively, increasing almost linearly as a function of the molar percentage of Tb_2O_3. ΔT ranges from 97–149 °C for the less concentrated samples and for the 27.5Tb40W sample it drops to 140 °C. This decrease is related to a lower stability of the glassy phase, tending towards a crystallized phase with higher concentrations of Tb_2O_3. For 20Tb40W and 22.5Tb40W samples, we observed two crystallization peaks, referring to $TbBO_3$ and $Tb_{11}O_{20}$ phases that form. As for the 25Tb40W and 27.5Tb40W samples, only a wider peak is observed, referring to the two phases crystallizing simultaneously.

One of the information that can be obtained using the density of the samples is the terbium ion effective concentration (N_{Tb3+}), that is, the effective amount of trivalent lanthanide ions that entered the structure of the glass matrix and contributes to the magneto-optical effect [38–40]. This ionic density is calculated using Eq. (2):

$$N_{Tb3+}\left(ion.cm^{-3}\right) = \frac{2x\rho N_A}{M} \quad (2)$$

Where x is the mole fraction of Tb_2O_3, N_A is the Avogadro constant, and M is the average molecular weight for each composition.

Theoretical optical basicity (Λ_{th}) is obtained from the Lewis acid-base theory and electronic polarizability [41–43] and is often used to determine the ability to donate electrons from oxygen in a glass matrix. It is used to classify the covalent/ionic ratios of the glasses since its value is inversely proportional to covalence. Λ_{th} can be correlated with the structural properties, such as an increase in non-bridging oxygens (NBO) generated by the introduction of a modifier in the glassy matrix, or with the optical constants refractive indices, and Verdet constants, due to the change in the polarizability [42,43]. According to Duffy [43,44] and Liu et al. [45]., a lower value of Λ_{th} reflects a lower content of NBO, so lower oxidation numbers of positively charged cations in the glass composition are consequently preferred, while higher Λ_{th} is related to higher refractive indices. The expression Eq. (3), proposed by Duffy, allows us to calculate the optical basicity.

$$\Lambda_{th} = \sum x_i \Lambda_i \quad (3)$$

Where the mole fraction for one of the glass precursors (x_i) and the theoretical intrinsic optical basicity value of an individual glass precursor (Λ_i) for B_2O_3, WO_3, Tb_2O_3, are respectively 0.425, 1.045 and 0.954 [46,47]. The variation of the Λ_{th} as a function of the terbium oxide content is better shown in Fig. 5, with lines drawn connecting specific points, acting as a guide for the eyes.

The Λ_{th} values increased as a function of the Tb_2O_3 concentration, passing from 0.922 to 0.938 from sample 20Tb40W to 27.5Tb40W respectively. This can be understood as an increasing in the NBO units due to the higher concentration of Tb^{3+}ions in the glass network. The addition of the Tb^{3+}ions together with the decrease of the boron oxide contributes to the depolymerization of the borotungstate chain in the glass, which is better observed and discussed in the structural properties analysis section. To summarize this set of characterizations, characteristic temperatures obtained by DSC, densities (ρ), terbium ion effective concentration (N_{Tb3+}) and theoretical optical basicity (Λ_{th}) are resumed in Table 2.

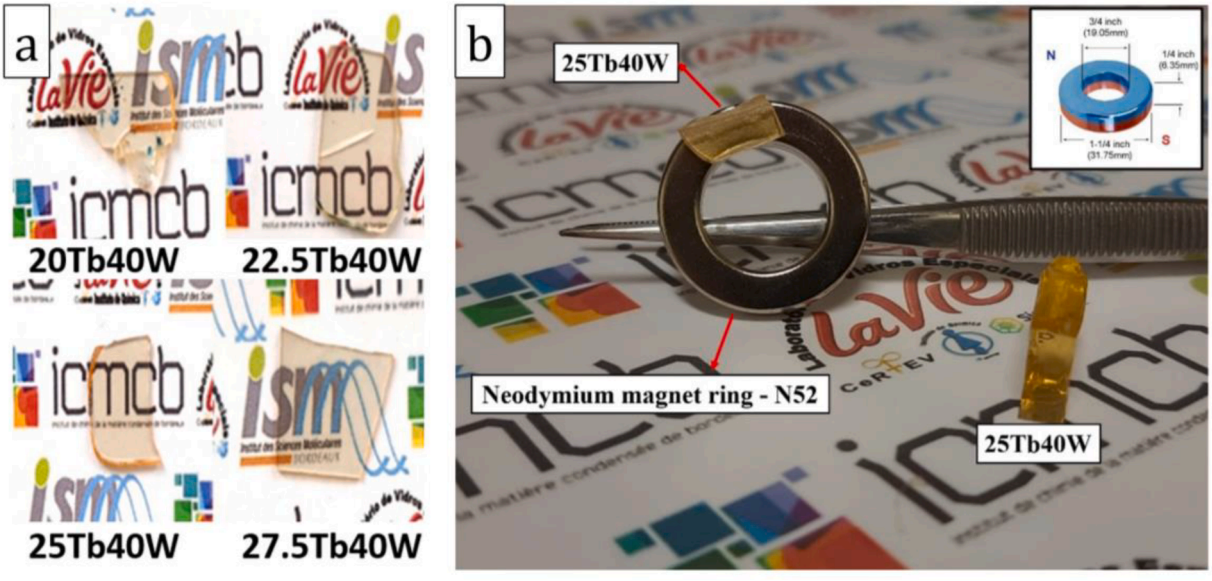

Fig. 2. a. Samples after cut and polishing with their respectives names. b. sample with 25 % mol Tb_2O_3 being attracted by a neodymium magnet ring (N52).

Table 1
Series of Tb-containing borotungstate glasses.

Samples	Nominal compositions (mol%)			Nominal compositions (cat mol%)			Phase separation after melt-quenching
	Tb_2O_3	WO_3	B_2O_3	$TbO_{3/2}$	WO_3	$BO_{3/2}$	
15Tb40W	15	40	45	18.75	25	56.25	Yes
20Tb40W	20	40	40	25	25	50	Non
22.5Tb40W	22.5	40	37.5	28.125	25	46.875	Non
25Tb40W	25	40	35	31.25	25	43.75	Non
27.5Tb40W	27.5	40	32.5	34.375	25	40.625	Non
30Tb40W	30	40	30	37.5	25	37.5	Yes

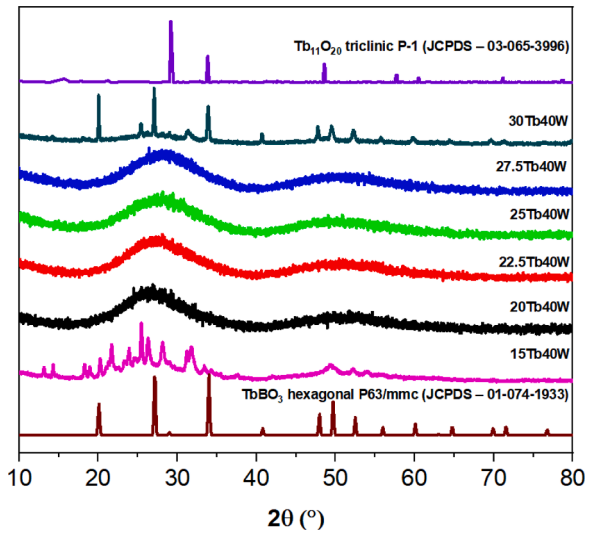

Fig. 3. XRD for the samples xTb40W, with the crystalline phases $TbBO_3$ hexagonal P63/mmc, analogous to $DyBO_3$ (JCPDS – 01-074-1933) and $Tb_{11}O_{20}$ P-1 triclinic (JCPDS – 03-065-3996).

3.2. Structural properties

Raman spectra of the samples xTb40W can be seen in Fig. 6a, with the respective bands attributions presented in Table 3. These Raman spectra are dominated by the tungsten associated modes at 350, 850 and 960 cm^{-1} as the polarizability of tungsten is much higher than that of boron. The boron structural units will be more easily determined by IR and ^{11}B- NMR. Fig. 6a also shows the Raman spectrum of the sample 25La40W used for comparison purposes.

The Raman spectra show three main regions. At low frequencies (200–600 cm^{-1}), it is possible to identify a broad band centered at ~350 cm^{-1} that can be assigned to a coupling of vibrations, including bending modes of $[WO_6]^{6-}$ octahedral [38,48–50], with the stretching modes of Tb-O [15,51,52]. In the region between 600 and 1000 cm^{-1}, there is an envelope, corresponding to W-O stretching modes. The large band at 720 and 850 cm^{-1} contains mainly the contributions from tungsten species in a 3D network, respectively W-O-W symmetric and asymmetric stretching modes of the distorted $[WO_6]^{6-}$ octahedral in non-crystalline lattices, while the ~950 cm^{-1} band refers to stretching mode of W-O^- having an ionic bonding with Tb^{3+}. The assignments of such bands have already been intensively discussed in the literature and they can be found in the following references [48,49,53,54]. According to Raman, there is a small variation in the relative intensity $\nu[W\text{-}O_t]^-$ / ν[W-O-W], regarding due to the increasing in the concentration of Tb^{3+} and consequent decreasing in B_2O_3. The higher concentration of $(WO_t)^-$ (~950 cm^{-1}) and consequently non-bridging oxygen (NBO), agrees with the data obtained for optical basicity.

As observed, the substitution of Tb^{3+} by La^{3+} does not seems to affect the structure of the glasses. It will be important, once NMR data cannot be obtained from terbium-containing glasses, due to its high paramagnetic behavior.

For a more accurate analysis of the contributions of boron

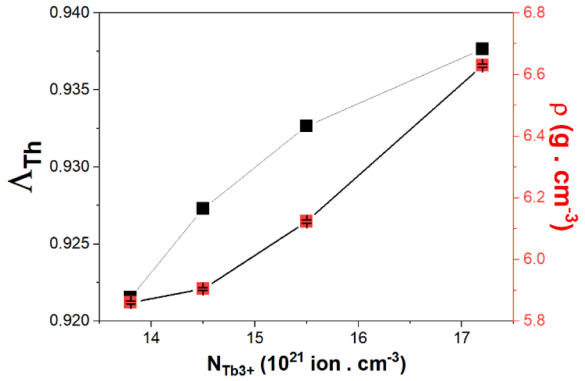

Fig. 5. Theoretical optical basicity (Λ_{th}) and density (ρ) for the samples varying the ion effective concentration of Tb^{3+}.

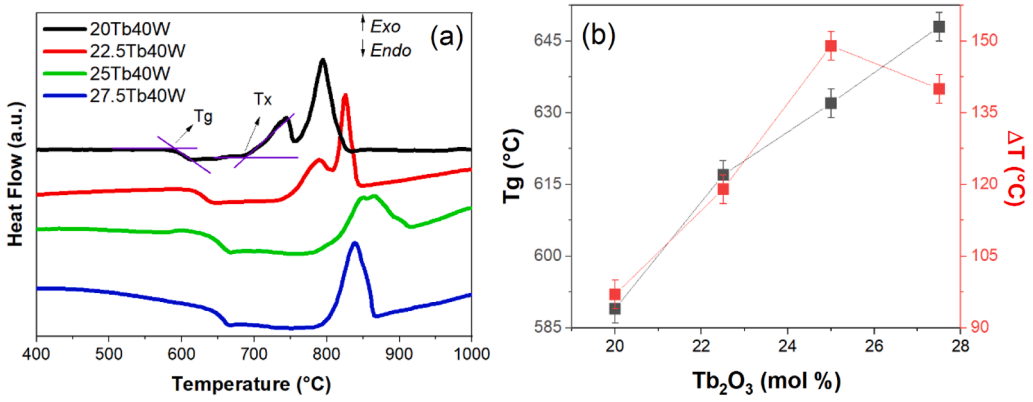

Fig. 4. a. DSCs curves and b. Tg and ΔT obtained for samples with different contents of Tb_2O_3 in the ternary system.

Table 2
Thermal and physical properties of the glass samples: Tg (glass transition temperature), Tx (onset of the crystallization temperature), ΔT (thermal stability parameter), ρ (density), N_{Tb3+} (terbium ion effective concentration) and Λ_{th} (theoretical optical basicity).

Samples	Tg (±3 °C)	Tx (±3 °C)	ΔT (±3 °C)	ρ (±0.005 g. cm^{-3})	N_{Tb3+} (10^{21} ion. cm^{-3})	Λ_{th}
20Tb40W	589	686	97	5.860	13.8	0.922
22.5Tb40W	617	736	119	5.904	14.5	0.927
25Tb40W	632	781	149	6.123	15.5	0.933
27.5Tb40W	648	788	140	6.629	17.2	0.938

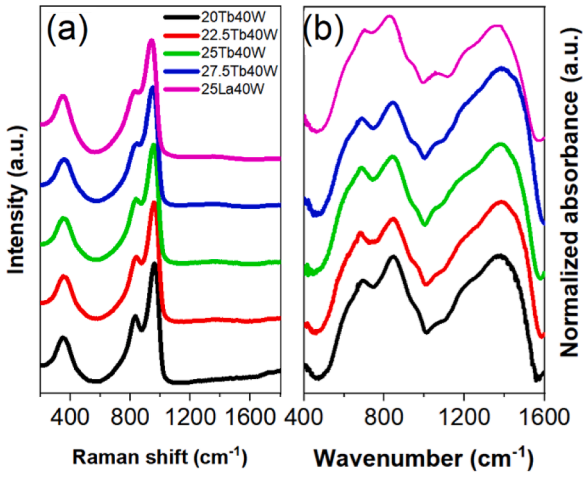

Fig. 6. a. Raman scattering spectroscopy and b. Normalized infrared absorption spectra, obtained by DRIFT, for xTb40W samples and 25La40W.

Table 3
Band assignments of the main vibrational modes for the xTb40W glasses.

Band observed (cm^{-1})	Raman	IR	Assignments	References
350	Yes	X	Coupling of δ $[WO_6]^{6-}$ units and ν Tb-O modes	[15,38, 48–52]
640–690	X	Yes	δ modes of BO_3 units	[15,33,51, 52,55]
760	Yes	Yes	ν_s W-O-W of the distorted $[WO_6]^{6-}$ octahedral in non-crystalline lattices	[38,48–50]
840	Yes	Yes	ν_{as} W-O-W of the distorted $[WO_6]^{6-}$ octahedral in non-crystalline lattices	
950	Yes	Yes	ν $(W\text{-}O_t)^-$ of the distorted $[WO_6]^{6-}$ octahedral in non-crystalline lattices	
1060	X	Yes	ν B-O of tetrahedral $[BO_4]^-$ units	[15,33,51,
1200–1500	X	Yes	ν modes of pyroborate $[B\text{Ø}O_2]^{2-}$ and metaborate $[B\text{Ø}_2O]^-$	52,55]

(Own authorship).

environment in the structural part, we have combined IR spectroscopy and ^{11}B-NMR analysis. However, as indicated above, terbium containing glasses cannot be investigated using NMR due to the paramagnetic response of the terbium ions which affect the magnetic response. To bypass such limitation, a glass with substitution of terbium by lanthanum was prepared with the composition $25La_2O_3$–$40WO_3$–$35B_2O_3$ (25La40W) which is suitable for NMR characterizations. Infrared spectrum for the composition 25La40W is reported in Fig. 6b together with the spectra of others terbium-containing samples. It can be observed that there are few differences between the spectra, suggesting that the Tb/La substitution presents only few structural changes. It denotes that the substitution allows some combined IR -NMR structural characterizations.

Fig. 7 shows the ^{11}B MAS-NMR spectrum of sample 25La40W, which can be described as the sum of four components associated with two different trigonal (BO_3) and two distinct tetragonal (BO_4) sites. Regarding the BO_3 environments, the two NMR signals are characterized by δ_{iso}= 16.9 ppm and δ_{iso}= 19.6 ppm and different quadrupolar parameters (C_Q and η). According to Stebbins et al. [56] these two sites could correspond to distorted trigonal site with one or two non-bridging oxygen, respectively. Note that the refined C_Q and η parameters extracted from the fitting of the NMR spectrum are also in accordance with the work of Stebbins et al.. The signals observed at lower NMR shift values are assigned to BO_4 environments [56]. Then, the relative proportion of BO_4 and BO_3 units was estimated to 34 % of boron in tetrahedral sites and 66 % in trigonal sites. Considering these results and the fact that the infrared response associated with boron in both lanthanum and terbium glasses are almost identical, one can assume that both 25Tb40W and 25La40W samples may present similar proportion of BO_4 and BO_3 environments.

Focusing on the IR spectra, Fig. 6b, the band around 640–690 cm^{-1}, can be assigned to bending vibrations of BO_3 units [15,33,51,52,55]. In the region between 760 and 840 cm^{-1}, attributed to ν_s and ν_{as} W-O-W from distorted $[WO_6]^{6-}$ octahedra, and shoulder in 960 cm^{-1} attributed to $\nu(W\text{-}O_t)^-$ of the distorted $[WO_6]^{6-}$ octahedra [38,48–50]. At 1060 cm^{-1}, the characteristic stretching modes of BO_4 units arises followed by bands in the region from 1200 to 1500 cm^{-1} that can be attributed to the BO_3 triangular structural units, being formed by pyroborate $[B\text{Ø}O_2]^{2-}$ and metaborate $[B\text{Ø}_2O]^-$, respectively [15,33,51,52,55]. The broadening of the band at 1200–1500 cm^{-1} can be attributed to a large dispersion of ionic interaction between Tb^{3+} ion and borate structural units. When the terbium concentration increase, the intensities of the bands attributed to meta and pyro trigonal borate units tends to increase relatively to the low frequency part of the spectra. It may indicate an increasing in the amount of non-bridging oxygen on borate trigonal units participating in the charge compensation of terbium ions, which is also in agreement with the optical basicity data.

The NMR, Raman and infrared spectroscopy analysis agree and have highlighted the importance of both tungsten and borate network on the environment of terbium ions within the glassy structure. This combined influence of both networks could be a key structural particularity to facilitate the incorporation of high concentration of rare earth ions.

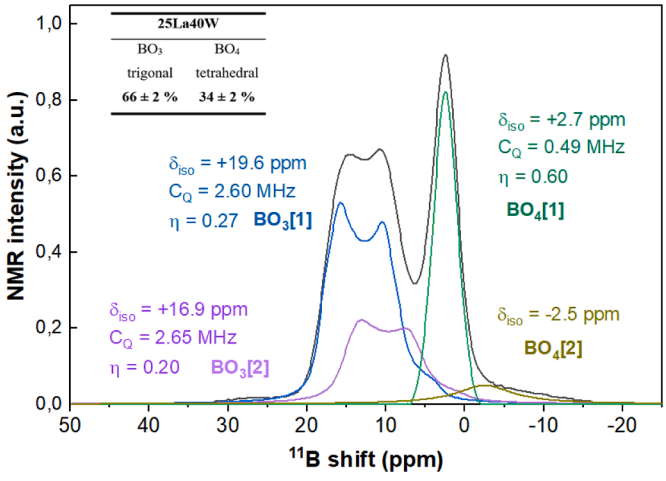

Fig. 7. ^{11}B MAS-NMR spectrum of the sample 25La40W, mimetizing sample 25Tb40W. (B_0=11.7 T, MAS rate 30 kHz).

3.3. Optical and luminescent properties

Fig. 8a shows the absorption coefficient of the terbium-containing samples, with the band gap energy values shown in Table 2. The absorption bands at 0.486, were assigned to the Tb^{3+} 4f–4f transitions from the $^7F_6$ ground state to the excited states $^5D_4$. The broad absorption band at $\lambda > 1.5$ μm corresponds to the $^7F_6 \rightarrow {}^7F_{0,1,2}$ transition of the Tb^{3+} ions [42,57–61]. The other characteristic absorptions of the Tb^{3+} ion of wavelengths smaller than 486 nm do not appear as they have higher energies than the band gap of the glasses [42]. The short wavelength cut-off (λ_{UV}) also increases from 357 to 388 nm for the 20Tb40W and 27.5Tb40W samples, respectively, due to structural changes, as seen in the previous section. The infrared cut-off starts with the presence of a shoulder referring to an absorption band around 3.7 μm.

Fig. 8b shows the luminescence (PL) spectra for the samples. The PL peaks, corresponding to 4f-4f transitions with excitation in 379 nm, at 415 ($^5D_3 \rightarrow {}^5F_5$), 440 ($^5D_3 \rightarrow {}^5F_4$), 487 ($^5D_4 \rightarrow {}^7F_6$), 543 ($^5D_4 \rightarrow {}^7F_5$), 583 ($^5D_4 \rightarrow {}^7F_4$), 621 ($^5D_4 \rightarrow {}^7F_3$), 652 ($^5D_4 \rightarrow {}^7F_2$), 667 ($^5D_4 \rightarrow {}^7F_1$) and 679 nm ($^5D_4 \rightarrow$ 7F0) [57–61]. The signal-to-noise intensity is low, allowing to identify transitions $^5D_3 \rightarrow {}^7F_J$ and $^5D_4 \rightarrow {}^7F_{2,1,0}$, of relative low intensity. It is observed that these samples present low luminescence intensities, not visible to the naked eyes, with few variations in intensities, indicating that the chemical environment for these Tb^{3+} concentrations does not show great differences, as revealed by the structural study. Low intensity is also characteristic of luminescence quenching effects, when high concentrations of the lanthanide ion allow the transfer of excitation energy between neighbours. For several glass systems, quenching can be observed above 3.0% in mol of Tb^{3+} and, for this system, we have 20 - 27.5% in mol of Tb_2O_3, extremely high concentrations to guarantee the paramagnetic effect in the matrix and, therefore, the quenching process was already expected. In addition, the energy difference of the $^5D_3 \leftrightarrow {}^5D_4$ and $^7F_0 \leftrightarrow {}^7F_6$ levels is very close (~5700 cm^{-1}), which allows the cross-relaxation quenching process between neighbouring Tb^{3+} to occur. Fig. 8d illustrates the excitation process for Tb^{3+} ions, the $^5D_4 \rightarrow {}^7F_J$ emissions and the cross-relaxation energy transfer process between Tb^{3+} ions. However, even if the rare earth element's concentration is high, weak radiative transitions from the $^5D_3$ level are still observed in the 400–480 nm range.

Fig. 8c shows the CIE 1931 chromaticity diagram, which uses the emission spectrum of the samples to determine the final emitted color. From this Figure, we observed that the emitted colours are concentrated in the same region of the graph, with small variations between the dots, illustrating that the luminescence spectra do not change considerably as a function of the concentration of Tb^{3+} ions.

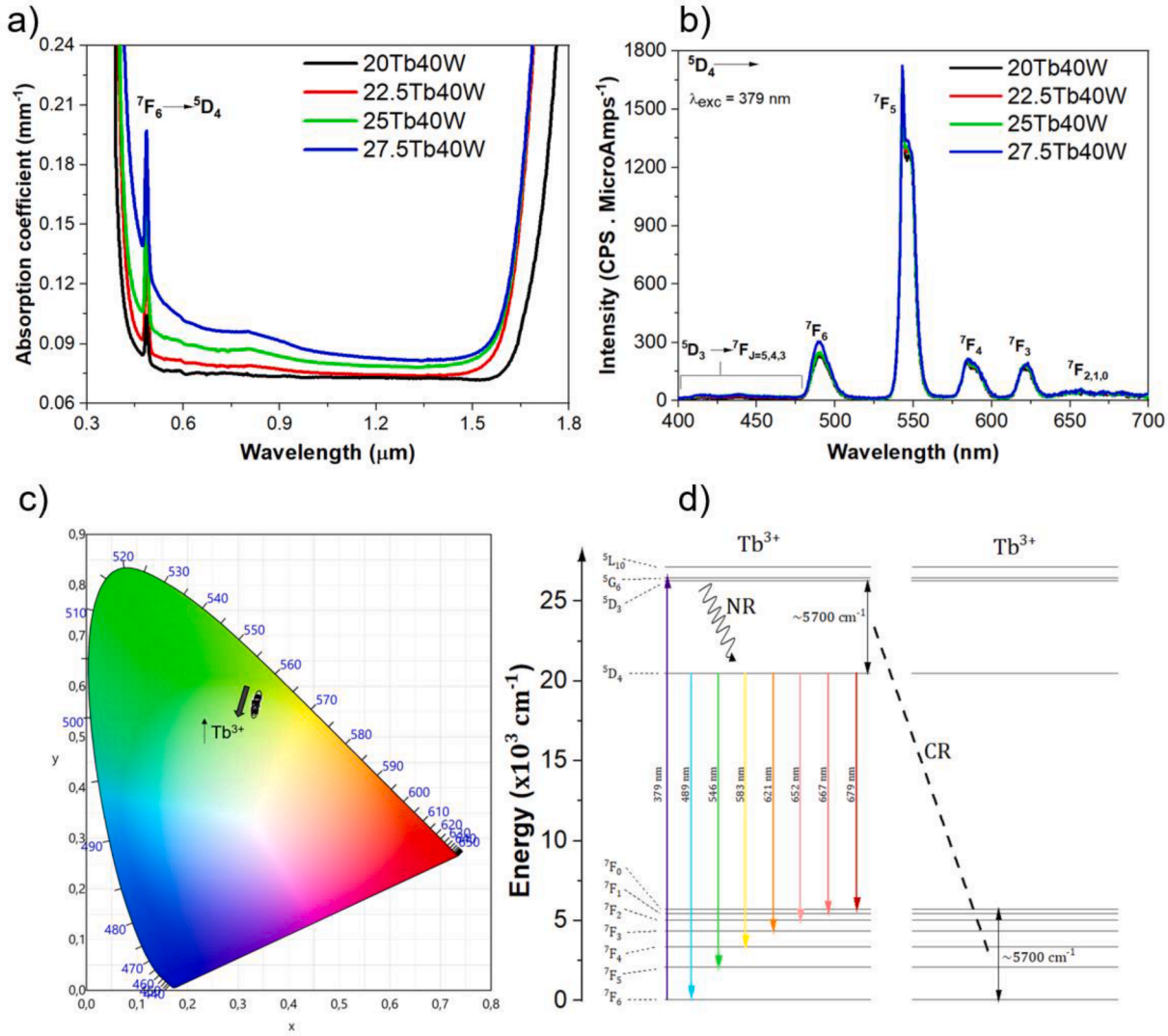

Fig. 8. a. Absorption coefficient spectra, b. Emission spectra showing the 4f- 4f ($^5D_4$ and $^5D_3 \rightarrow$) transitions under $\lambda_{exc} = 379$ nm., c. CIE 1931 chromaticity diagram for samples xTb40W, and d. Partial energy level diagram of Tb^{3+} illustrating the excitation $^7F_6 \rightarrow {}^5D_3 + {}^5G_6$, non-radiative decay (NR; $^5D_3 \rightarrow {}^5D_4$), emissions $^5D_4 \rightarrow {}^7F_J$, and cross-relaxation process (CR) between two neighbouring Tb^{3+} ions.

3.4. Magnetic properties

Eqs. (5) and (6) presents the dependencies of Verdet constant, that can be evaluated by presents diamagnetic (V_{dia}) and paramagnetic (V_{para}) contributions, respectively.

$$V_{dia} = \left(\frac{e\nu}{m_e c}\right)\frac{dn}{d\nu} \tag{5}$$

where e is the elementary charge, m_e is the mass of the electron, c is the speed of light, ν is the frequency of the incident light, and $dn/d\nu$ is the refractive index dispersion [41,62,63].

$$V_{para} = \left(\frac{4\pi^2}{ch\mu_B N_A}\right)\frac{N_R \nu^2}{g}\chi_{para}\sum_n \frac{C_n}{(\nu^2 - \nu_n{}^2)} \tag{6}$$

where h is the Planck constant, N_R is the number of paramagnetic species (R) per unit volume (R . cm^{-3}), C_n is related to the transition probabilities, ν_n is the transition frequencies, μ_B is Bohr magneton, g is Landé g-factor, and χ_{para} is the paramagnetic susceptibility [41,64–66].

It is expected that glasses with high concentrations of terbium have a relevant paramagnetic contribution, therefore, the study of magnetic susceptibility becomes interesting for the magneto-optical study, since χ is directly proportional to V.

Fig. 9 shows the temperature dependence of the magnetic molar susceptibility χ_{para}. An asymptotic behavior when the temperature tends to 0 K is observed, which is consistent with the paramagnetic behavior. Total molar magnetic susceptibility comes from the sum of diamagnetic contributions (χ_{dia}) and paramagnetic contributions (χ_{para}) of each sample, as shown in Eq. (7):

$$\chi_M = \chi_{para} + \chi_{dia} \tag{7}$$

Diamagnetic susceptibilities were calculated according to Bain and Berry [67], which takes into account the mol% of each atom present in the Tb_2O_3-B_2O_3-WO_3 system and their respective tabulated values of diamagnetic susceptibility of each atom.

The refined values of the constants for the terbium samples are shown in Table 4. In the inset of Fig. 9 is shown the inverse of paramagnetic susceptibility ($1/\chi$) versus temperature, varying linearity, which demonstrates that the samples follow the Curie-Weiss law [64,68,69], like Eq. (8) which is used to determine these characteristic constants with the intercept and slope of the linear fit.

$$\frac{1}{\chi_{para}} = \frac{1}{C}.T + \left(-\frac{\theta}{C}\right) \tag{8}$$

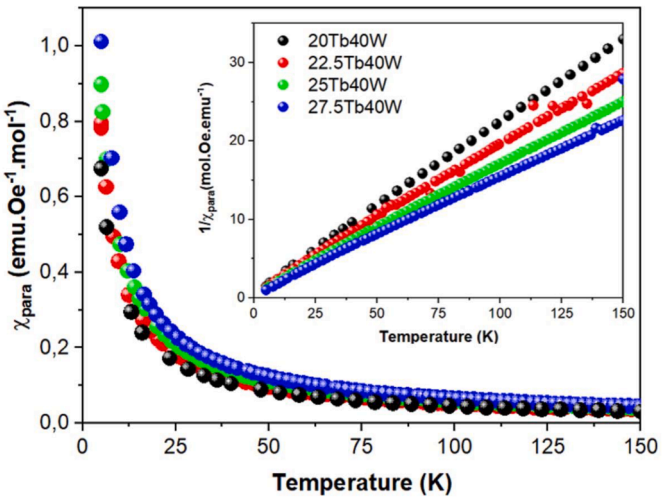

Fig. 9. Temperature dependence of the paramagnetic molar susceptibility for all samples.

where C is the Curie constant, and θ is the Weiss temperature. The Curie constant value can be used as a method of verifying the concentration of Tb^{3+} ions in the samples, based on the targeted chemical composition, comparing the calculated Curie constant with experimental. The calculation of the Curie constant will depend on the total magnetic moment of the ion (J), which in turns depends on the ground state of each ion. Eq. (9) shows respectively those relations.

$$C = \frac{\mu_B{}^2}{3\,k_B}.\,\mu_{eff}{}^2 = \frac{1}{8}.\,g_J{}^2[J(J+1)] \tag{9}$$

where k_B is the Boltzmann constant, μ_B is the Bohr magneton, μ_{eff} is the disordered state total magnetic moment, J is the total angular momentum quantum number and g_J is the Landé g-factor, which is also a term dependent on the ground state of each ion, as shown in the Eq. (10).

$$g_J = 1 + \frac{J(J+1) + S(S+1) - L(L+1)}{2J(J+1)} \tag{10}$$

where S and L are quantum numbers describing the total spin angular momentum, and total orbital angular momentum, respectively.

For Tb^{3+}, its fundamental level is $^7\mathbf{F_6}$, and, redoing the calculations, we obtain a $gJ = 1.50$, $\mu_{eff} = 9.72$ and $C = 11.81$ emu.K.Oe.mol-1. From the theoretic value of C, we can probed the percentage of ions Tb^{3+} and Tb_2O_3 present in the samples, also shown in Table 4, with the percentage of error of the expected value during the synthesis and the probed after the magnetic susceptibility measurement and the related calculations.

It is noted that the differences between the expected and calculated ranged from 0.82- 5.78 % for the glassy samples show a good correlation between targeted and experimental values. This is correlated with the increase in paramagnetic species in the glass. The θ, on the other hand, has a nonlinear behavior, decreasing with terbium concentration up to the 25Tb40W sample and increasing again for the more concentrated samples. The high values of the Curie constant reveal that the samples have high magnetic susceptibility. As discussed earlier, negative Weiss temperature values indicate that the spins are aligned antiparallel, causing low antiferromagnetic interactions.

Inset shown the inverse of susceptibility ($1/\chi_{para}$) versus temperature, varying linearity and follow the Curie-Weiss law.

The results from our study reveal elevated susceptibility values in comparison to those found in the literature. Table 5 presents the Curie constants and Weiss temperature values for the glass samples discussed in this article, juxtaposed with corresponding values from existing literature. The tellurite [70], iron-phosphate [71,72], iron-aluminoborate [73] and aluminosilicate [74] glasses presented comparable or higher values, but these glasses do not have good transparency in the visible region, reducing their range of applications for MO devices.

3.5. Magneto-optical properties

In this work the Verdet constant values (V, rad.T^{-1}m^{-1}) were obtained experimentally, using the Faraday effect, using the relation showed in Eq. (11).

$$\beta = B\,.\,l\,.\,V \tag{11}$$

where B is the magnetic field, l is the optical path and β was the average of 5 measurements for the angle of light rotation after the application of a magnetic field (0.13T).

In Fig. 10a, the Verdet constant values for some reference crystals and several Tb-containing glasses are presented [9,12,23,77–79] using lasers in the 630–650 nm range. As observed, the magneto-optical effect tends to increase linearly with increasing of N_{Tb3+}, with a dotted line drawn demonstrating this tendency. Fluoride glasses [80] have the lowest N_{Tb3+}values, reflecting, proportionally, the smaller Verdet constant. The Verdet values increase from phosphate glasses [24,62],

Table 4
Theoretical diamagnetic susceptibility (χ_{dia}), Weiss temperature (θ), Curie constant (C) for two units systems (cgs in Oested, Oe, e SI in Tesla, T) and probed Tb_2O_3% mol for each sample.

Samples	χ_{dia} ($*10^{-6}$ emu.mol^{-1})	θ (K)	C (emu . Oe^{-1} . mol^{-1})	C (A . m^2 . T^{-1} . mol^{-1})	[Tb_2O_3] (% mol) targeted	probed	error%
20Tb40W	−48.96	−4.28	4.68	46.76	20	19.79	1.04
22.5Tb40W	−49.90	−4.67	5.36	53.59	22.5	22.69	−0.82
25Tb40W	−50.84	−6.51	6.25	62.48	25	26.45	−5.78
27.5Tb40W	−51.78	−4.38	6.77	67.66	27.5	28.64	−4.15

Table 5
Comparison between different Curie constant (C) values and Weiss temperature (θ) for samples from this work and examples from the literature.

Glass matrix	Concentration paramagnetic species (% mol)	C (emu . Oe^{-1} . mol^{-1})	θ (K)	References
Borotungstate	27.5 % Tb_2O_3	6.77	−4.38	This work
	25 % Tb_2O_3	6.25	−6.51	
	22.5 % Tb_2O_3	5.36	−4.67	
	20 % Tb_2O_3	4.68	−4.28	
Borogermanate	10 % Tb_4O_7	4.29	−0.869	[1]
Borogermanate	20 % Gd_2O_3	3.124	−1.56	[2]
Gallogermanate	25 % Gd_2O_3	3.311	35.34	[17]
Aluminophosphate	9.52 % Dy_2O_3	3.66	X	[75]
Iron tellurite	25 % MnO_2	7.28	−5.098	[70]
Iron phosphate	43 % Fe_2O_3 (wt%)	3.98	−54	[71]
Iron phosphate	57.1 % FeO	4.82	−11.6	[72]
Iron aluminoborate	20 % Gd_2O_3	8.2	−3.2	[73]
Aluminosilicate	11.8 % Co	5.61125	−95	[74]
	12.3 % Mn	6.0552	−194	
Boromolibdate	21.25 % Gd_2O_3	1.672	−0.7	[76]

passing for fluorophosphates glasses [23,62,80,81], aluminosilicate glasses [62,65,82–84], borate glasses [62,80,85,86] and borosilicates [84,87–89]. Currently, the glasses with the highest N_{Tb3+} and, consequently, the highest Verdet constant, are borogermanate [1,16,42,90,91] and borogermanosilicate glasses [18,41,92–94]. The results obtained for the glasses studied in present work are shown as red squares. The Verdet constants obtained for samples 20Tb40W, 22.5Tb40W, 25Tb40W and 27.5Tb40W were −60, −71, −91 and −124 rad.T^{-1}m^{-1}, respectively. Those glasses present high verdet constant and are also of interest for producing cost issues. Indeed, borotungstate are approximately 10 times cheaper to be produced compared to borogermanate due to the high cost of germanium oxide. Besides that, borotungstate are prepared in lower temperatures (1350 °C) while borogermanate need temperatures around 1500–1550 °C depending on the content of terbium oxide.

Fig. 10b shows the same graph V versus N_{Tb3+}, but focused only on the samples of this work, comparing them with monocrystals containing terbium used as commercial Faraday rotators. Lines were drawn connecting specific points as a guide for the eyes. The samples of this study exhibit high Verdet constant values, very close to the commercial crystal TGG and borogermanate glasses, being, therefore, materials with high relevance in the field of magneto-optics.

3.6. Conclusion

In summary, we have reported the synthesis and characterizations of high Tb_2O_3 content borotungstate glasses. A very limited glass forming domain has been determined and a complete structural analysis tends to point out the combined influence of borate and tungstate networks on the environment of terbium ions. This structural aspect could facilitate the glass formation at such high loading of rare earth ions. Even at high concentrations, characteristic emissions of the Tb^{3+} ion can be determined, also opening space for multifunctional applications.

Their magnetic properties showed high Curie constant values, unprecedented for a borotungstate system and even high compared to literature. Weiss temperature demonstrated that the studied system presents antiparallel spin alignment. The values obtained for the magneto-optical constant, V, exhibit an unprecedented occurrence within borotungstate system, and are comparable to commercial magneto-optical materials, such as borogermanate glasses and

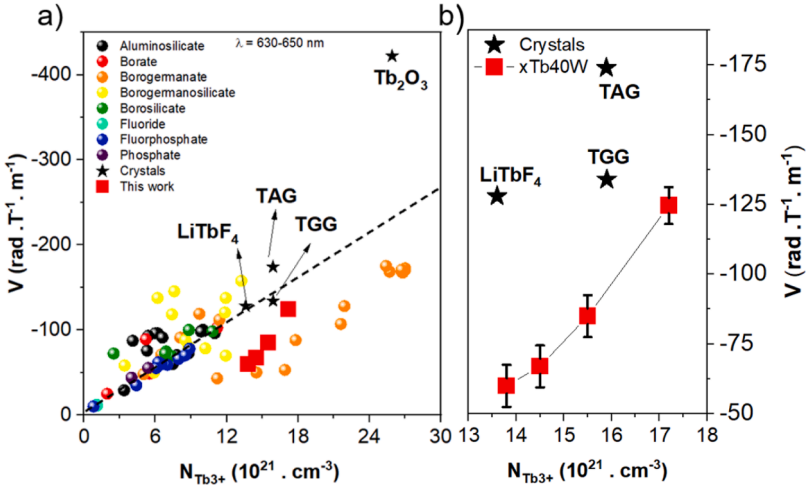

Fig. 10. a. Variation of the Verdet constant by concentration of Tb^{3+}ions for the samples (red squares), some reference crystals (black stars) and different glass families (spheres): aluminosilicates (black), borates (red), borogermanates (orange), borogermanosilicates (yellow), borosilicates (green), fluorides (turquoise), fluorophosphates (blue) and phosphates glasses (purple). **b.** Behavior of the Verdet constant of the xTb40W samples of this work (red squares) compared with commercially used crystals (black stars). (For interpretation of the references to color in this figure legend, the reader is referred to the web version of this article.)

monorystals, being a cheaper replacement alternative for magneto-optical devices operating from the visible up to the middle infrared, including the telecom range, optical switchers, and even magneto-optical sensors.

CRediT authorship contribution statement

Leonardo Vieira Albino: Conceptualization, Data curation, Investigation, Methodology, Writing – original draft. **Marc Dussauze:** Data curation, Formal analysis, Investigation, Writing – review & editing. **Olivier Toulemonde:** Data curation, Formal analysis, Investigation, Writing – review & editing. **Mathieu Duttine:** Data curation, Formal analysis, Investigation, Writing – review & editing. **Véronique Jubera:** Data curation, Formal analysis, Investigation, Writing – review & editing. **Douglas Faza Franco:** Data curation, Formal analysis, Investigation, Writing – review & editing. **Thierry Cardinal:** Data curation, Formal analysis, Funding acquisition, Investigation, Supervision, Writing – review & editing. **Marcelo Nalin:** Conceptualization, Data curation, Formal analysis, Funding acquisition, Investigation, Supervision, Writing – review & editing.

Declaration of competing interest

The authors declare there is no conflict of interests.

Data availability

Data will be made available on request.

Acknowledgements

The authors acknowledge Coordination for the Improvement of Higher Education Personnel Internationalization Program (CAPES-Print, grant 88887.571031/2020-00 and 88882.330082/2019-01), São Paulo Research Foundation (FAPESP, grant 2013/07793-6), acknowledges FUNGLASS Project, funding received from the European Union's Horizon 2020 research and innovation program under the Marie Skłodowska-Curie grant agreement No. 823941, French National Centre for Scientific Research (CNRS), Bordeaux INP and National Council for Scientific and Technological Development (CNPq).

References

[1] D.F. Franco, R.G. Fernandes, J.F. Felix, V.R. Mastelaro, H. Eckert, C.R.M. Afonso, Y. Messaddeq, S.H. Messaddeq, S. Morency, M. Nalin, Fundamental studies of magneto-optical borogermanate glasses and derived optical fibers containing Tb3+, J. Mater. Res. Technol. 11 (2021) 312–327, https://doi.org/10.1016/j.jmrt.2021.01.010.

[2] R.G. Fernandes, D.F. Franco, V.R. Mastelaro, T. Cardinal, O. Toulemonde, M. Nalin, Thermal and structural modification in transparent and magnetic germanoborate glasses induced by Gd_2O_3, Ceram. Int. 46 (2020) 22079–22089, https://doi.org/10.1016/j.ceramint.2020.05.227.

[3] Q. Chen, WO_3 concentration-dependent magneto-optical properties of Faraday rotating glasses and glass-ceramics, J. Non. Cryst. Solids 522 (2019) 119584, https://doi.org/10.1016/j.jnoncrysol.2019.119584.

[4] M. Mollaee, X. Zhu, S. Jenkins, J. Zong, E. Temyanko, R. Norwood, A. Chavez-Pirson, M. Li, D. Zelmon, N. Peyghambarian, Magneto-optical properties of highly Dy 3+ doped multicomponent glasses, Opt. Express. 28 (2020) 11789, https://doi.org/10.1364/oe.392008.

[5] P. Zu, C.C. Chan, L.W. Siang, Y. Jin, Y. Zhang, L.H. Fen, L. Chen, X. Dong, Magneto-optic fiber Sagnac modulator based on magnetic fluids, Opt. Lett. 36 (2011) 1425, https://doi.org/10.1364/ol.36.001425.

[6] T.L.S. Collaboration, Advanced LIGO, Class. Quantum Gravity. 32 (2015), https://doi.org/10.1088/0264-9381/32/7/074001.

[7] J. Qin, S. Xia, W. Yang, H. Wang, W. Yan, Y. Yang, Z. Wei, W. Liu, Y. Luo, L. Deng, L. Bi, Nanophotonic devices based on magneto-optical materials: recent developments and applications, Nanophotonics 11 (2022) 2639–2659, https://doi.org/10.1515/nanoph-2021-0719.

[8] J. Dai, J. Li, Promising magneto-optical ceramics for high power Faraday isolators, Scr. Mater. 155 (2018) 78–84, https://doi.org/10.1016/J.SCRIPTAMAT.2018.06.031.

[9] P. Veber, M. Velázquez, G. Gadret, D. Rytz, M. Peltz, R. Decourt, Flux growth at 1230 °c of cubic Tb_2O_3 single crystals and characterization of their optical and magnetic properties, CrystEngComm 17 (2015) 492–497, https://doi.org/10.1039/c4ce02006e.

[10] M. Geho, T. Sekijima, T. Fujii, Growth of terbium aluminum garnet ($Tb_3Al_5O_{12}$; TAG) single crystals by the hybrid laser floating zone machine, J. Cryst. Growth. 267 (2004) 188–193, https://doi.org/10.1016/j.jcrysgro.2004.03.068.

[11] M.Y.A. Raja, D. Allen, W. Sisk, Room-temperature inverse Faraday effect in terbium gallium garnet, Appl. Phys. Lett. 67 (1995) 2123, https://doi.org/10.1063/1.114740.

[12] D. Vojna, O. Slezák, A. Lucianetti, T. Mocek, Verdet constant of magneto-active materials developed for high-power Faraday devices, Appl. Sci. 9 (2019), https://doi.org/10.3390/app9153160.

[13] M.R. Prakash, G. Neelima, V.K. Kummara, N. Ravi, C.D. Viswanath, T.S. Rao, S. M. Jilani, Holmium doped bismuth-germanate glasses for green lighting applications: a spectroscopic study, Opt. Mater. 94 (2019) 436–443, https://doi.org/10.1016/j.optmat.2019.05.003.

[14] M. Zagrai, M. Unguresan, S. Rada, J. Zhang, M. Pica, E. Culea, Local structure in gadolinium-lead-borate glasses and glass-ceramics, J. Non. Cryst. Solids 546 (2020) 120259, https://doi.org/10.1016/j.jnoncrysol.2020.120259.

[15] S. Sasaki, A. Masuno, K. Ohara, Y. Yanaba, H. Inoue, Y. Watanabe, S. Kohara, Structural origin of additional infrared transparency and enhanced glass-forming ability in rare-earth-rich borate glasses without B-O networks, Inorg. Chem. 59 (2020) 13942–13951, https://doi.org/10.1021/acs.inorgchem.0c01567.

[16] L. Zhou, Z. Zhu, Study of magneto-optical properties of GeO_2-B_2O_3-P_2O_5-ZnO-Tb_2O_3 glass doped with different rare-earth ions, J. Non. Cryst. Solids 576 (2022) 121241, https://doi.org/10.1016/j.jnoncrysol.2021.121241.

[17] R. Zaiter, M. Dussauze, M. Nalin, E. Fargin, F. Adamietz, S. Danto, O. Toulemonde, T. Cardinal, Thermal and structural modification in transparent and magnetic gallogermanate glasses induced by Gd_2O_3, J. Alloys Compd. 912 (2022) 165181, https://doi.org/10.1016/j.jallcom.2022.165181.

[18] H. Yin, Y. Gao, H. Guo, C. Wang, C. Yang, Effect of B_2O_3 content and microstructure on Verdet constant of Tb_2O_3-doped GBSG magneto-optical glass, J. Phys. Chem. C. 122 (2018) 16894–16900, https://doi.org/10.1021/acs.jpcc.8b04989.

[19] H. Lin, H. Yang, L. Zhou, J. He, B. Liu, N. Li, C. Li, S. Li, W. Yang, X. Jiang, H. Liu, F. Zeng, Z. Su, Research on the physical and optical properties of Dy3+ doped 30 mol%Tb_2O_3–B_2O_3-GeO_2-PbO-SiO_2 magneto-optical glass with high Verdet constant, J. Phys. Chem. Solids 166 (2022) 110682, https://doi.org/10.1016/J.JPCS.2022.110682.

[20] S. Ju, J. Kim, K. Linganna, P.R. Watekar, S.G. Kang, B.H. Kim, S. Boo, Y. Lee, Y. H. An, C.J. Kim, W.T. Han, Temperature and vibration dependence of the Faraday effect of Gd_2O_3 NPs-doped alumino-silicate glass optical fiber, Sensors 18 (2018) 1–13, https://doi.org/10.3390/s18040988.

[21] V.D. Dubrovin, X. Zhu, M. Mollaee, J. Zong, N. Peyghambarian, Highly Dy_2O_3 and Er_2O_3 doped boron-aluminosilicate glasses for magneto-optical devices operating at 2μm, J. Non. Cryst. Solids 569 (2021) 120986, https://doi.org/10.1016/J.JNONCRYSOL.2021.120986.

[22] M. Elisa, R. Stefan, I.C. Vasiliu, M.I. Rusu, B.A. Sava, L. Boroica, M. Sofronie, V. Kuncser, A.C. Galca, A. Beldiceanu, A. Volceanov, M. Eftimie, Thermal, structural, magnetic and magneto-optical properties of dysprosium-doped phosphate glass, J. Non. Cryst. Solids 521 (2019) 119545, https://doi.org/10.1016/J.JNONCRYSOL.2019.119545.

[23] B. Bellanger, Y. Ledemi, Y. Messaddeq, Fluorophosphate glasses with high terbium content for magneto-optical applications, J. Phys. Chem. C. 124 (2020) 5353–5362, https://doi.org/10.1021/acs.jpcc.9b11696.

[24] A. Babkina, E. Kulpina, Y. Sgibnev, Y. Fedorov, A. Starobor, O. Palashov, N. Nikonorov, A. Ignatiev, K. Zyryanova, K. Oreshkina, E. Zhizhin, D. Pudikov, Terbium concentration effect on magneto-optical properties of ternary phosphate glass, Opt. Mater. 100 (2020) 109692, https://doi.org/10.1016/j.optmat.2020.109692.

[25] R.M. Abdelouhab, R. Braunstein, K. Bärner, Identification of tungstate complexes in lithium-tungstate-borate glasses by Raman spectroscopy, J. Non. Cryst. Solids 108 (1989) 109–114, https://doi.org/10.1016/0022-3093(89)90338-4.

[26] M. Ataalla, A.S. Afify, M. Hassan, M. Abdallah, M. Milanova, H.Y. Aboul-Enein, A. Mohamed, Tungsten-based glasses for photochromic, electrochromic, gas sensors, and related applications: a review, J. Non. Cryst. Solids 491 (2018) 43–54, https://doi.org/10.1016/j.jnoncrysol.2018.03.050.

[27] Y. Taki, K. Shinozaki, T. Honma, T. Komatsu, L. Aleksandrov, R. Iordanova, Coexistence of nano-scale phase separation and micro-scale surface crystallization in Gd_2O_3-WO_3-B_2O_3 glasses, J. Non. Cryst. Solids 381 (2013) 17–22, https://doi.org/10.1016/j.jnoncrysol.2013.09.014.

[28] N. Wantana, E. Kaewnuam, Y. Ruangtaweep, D. Valiev, S. Stepanov, K. Yamanoi, H.J. Kim, J. Kaewkhao, Radio, cathodo and photoluminescence investigations of high density WO_3-Gd_2O_3-B_2O_3 glass doped with Tb3+, Radiat. Phys. Chem. 164 (2019) 108350 https://doi.org/10.1016/j.radphyschem.2019.108350.

[29] N. Wantana, E. Kaewnuam, H.J. Kim, S.C. Kang, Y. Ruangtaweep, S. Kothan, J. Kaewkhao, X-ray/proton and photoluminescence behaviors of Sm3+ doped high-density tungsten gadolinium borate scintillating glass, J. Alloys Compd. 849 (2020) 156574, https://doi.org/10.1016/j.jallcom.2020.156574.

[30] W. Rittisut, N. Wantana, Y. Ruangtaweep, P. Mool-am-kha, J. Padchasri, S. Rujirawat, P. Manyum, R. Yimnirun, P. Kidkhunthod, A. Prasatkhetragarn, S. Kothan, H.J. Kim, J. Kaewkhao, Bright white light emission from (Gd3+ /Dy3+) dual doped transparent lithium aluminum borate glasses for W- LED application, Opt. Mater. 122 (2021) 111705, https://doi.org/10.1016/j.optmat.2021.111705.

[31] N. Wantana, E. Kaewnuam, Y. Ruangtaweep, P. Kidkhunthod, H.J. Kim, S. Kothan, J. Kaewkhao, High density tungsten gadolinium borate glasses doped with Eu3+ ion for photonic and scintillator applications, Radiat. Phys. Chem. 172 (2020) 108868, https://doi.org/10.1016/j.radphyschem.2020.108868.
[32] N. Wantana, E. Kaewnuam, Y. Ruangtaweep, D. Valiev, S. Stepanov, K. Yamanoi, H.J. Kim, S. Kothan, J. Kaewkhao, Tunable orange, yellow and white emission of Pr3+-doped tungsten gadolinium borate glasses, J. Non. Cryst. Solids 554 (2021) 120603, https://doi.org/10.1016/j.jnoncrysol.2020.120603.
[33] E.I. Kamitsos, A.P. Patsis, M.A. Karakassides, G.D. Chryssikos, Infrared reflectance spectra of lithium borate glasses, J. Non. Cryst. Solids 126 (1990) 52–67, https://doi.org/10.1016/0022-3093(90)91023-K.
[34] W. Blanc, Y. Gyu Choi, X. Zhang, M. Nalin, K.A. Richardson, G.C. Righini, M. Ferrari, A. Jha, J. Massera, S. Jiang, J. Ballato, L. Petit, The past, present and future of photonic glasses: a review in homage to the United Nations International Year of glass 2022, Prog. Mater. Sci. 134 (2023) 101084, https://doi.org/10.1016/j.pmatsci.2023.101084.
[35] A.K. Varshneya, J.C. Mauro, Fundamentals of Inorganic Glasses, 3rd ed., Elsevier, 2019.
[36] J.E. Shelby, Introduction to glass science and technology, R. Soc. Chem. (1997), https://doi.org/10.1039/9781847551160.
[37] E.M. Levin, R.S. Roth, J.B. Martin, Polymorphism of AbO_3 type rare earth borates*, Am. Mineral. 46 (1961) 1030–1055. ISSN: 1945-3027.
[38] L. Aleksandrov, T. Komatsu, R. Iordanova, Y. Dimitriev, Raman spectroscopic study of structure of $WO_3La\ 2O_3B_2O_3$ glasses with no color and crystallization of LaBWO6, Opt. Mater. 34 (2011) 201–206, https://doi.org/10.1016/j.optmat.2011.08.002.
[39] Y. Wang, T. Honma, T. Komatsu, Effects of WO_3 substitution on crystallization behavior and laser patterning in Gd_2O_3-MoO_3-B_2O_3 glasses, J. Non. Cryst. Solids 383 (2014) 86–90, https://doi.org/10.1016/j.jnoncrysol.2013.04.016.
[40] L. Aleksandrov, T. Komatsu, K. Shinozaki, T. Honma, R. Iordanova, Structure of MoO_3-WO_3-La_2O_3-B_2O_3 glasses and crystallization of LaMo1 - XWxBO6 solid solutions, J. Non. Cryst. Solids 429 (2015) 171–177, https://doi.org/10.1016/j.jnoncrysol.2015.09.004.
[41] H. Yang, Z. Zhu, Magneto-optical glass mixed with Tb3+ ions: high Verdet constant and luminescence properties, J. Lumin. 231 (2021) 117804, https://doi.org/10.1016/j.jlumin.2020.117804.
[42] D.F. Franco, Y. Ledemi, W. Correr, S. Morency, C.R.M. Afonso, S.H. Messaddeq, Y. Messaddeq, M. Nalin, Magneto-optical borogermanate glasses and fibers containing Tb3+, Sci. Rep 11 (2021) 1–16, https://doi.org/10.1038/s41598-021-89375-1.
[43] J.A. Duffy, A review of optical basicity and its applications to oxidic systems, Geochim. Cosmochim. Acta. 57 (1993) 3961–3970, https://doi.org/10.1016/0016-7037(93)90346-X.
[44] J.A. Duffy, Optical basicity: a practical acid-base theory for oxides and oxyanions, J. Chem. Educ. 73 (1996) 1138–1142, https://doi.org/10.1021/ed073p1138.
[45] S. Liu, G. Zhao, W. Ruan, Z. Yao, T. Xie, J. Jin, H. Ying, J. Wang, G. Han, Reduction of Eu3+ to Eu2+ in aluminoborosilicate glasses prepared in air, J. Am. Ceram. Soc. 91 (2008) 2740–2742, https://doi.org/10.1111/j.1551-2916.2008.02496.x.
[46] V. Dimitrov, T. Komatsu, Classification of simple oxides: a polarizability approach, J. Solid State Chem. 163 (2002) 100–112, https://doi.org/10.1006/jssc.2001.9378.
[47] X. Zhao, X. Wang, H. Lin, Z. Wang, Electronic polarizability and optical basicity of lanthanide oxides, Phys. B 392 (2007) 132–136, https://doi.org/10.1016/j.physb.2006.11.015.
[48] J.F.V.L. Munhoz, S.H. Santagneli, M. de Oliveira, A.C.M. Rodrigues, H. Eckert, M. Nalin, Glasses in the $NaPO_3$-WO_3-NaF ternary system: preparation, physical properties and structural studies, J. Non. Cryst. Solids 505 (2019) 379–389, https://doi.org/10.1016/J.JNONCRYSOL.2018.10.043.
[49] G. Poirier, Y. Messaddeq, S.J.L. Ribeiro, M. Poulain, Structural study of tungstate fluorophosphate glasses by Raman and X-ray absorption spectroscopy, J. Solid State Chem. 178 (2005) 1533–1538, https://doi.org/10.1016/j.jssc.2004.10.032.
[50] A.K. Yadav, P. Singh, A review of structure of oxide glasses by Raman spectroscopy, RSC Adv 5 (2015) 67583–67609, https://doi.org/10.1039/C5RA13043C.
[51] B. Topper, N.S. Tagiara, A. Herrmann, E.I. Kamitsos, D. Mönсke, Yttrium and rare-earth modified lithium orthoborates: glass formation and vibrational activity, J. Non. Cryst. Solids (2022) 575, https://doi.org/10.1016/j.jnoncrysol.2021.121152.
[52] C.P.E. Varsamis, N. Makris, C. Valvi, E.I. Kamitsos, Short-range structure, the role of bismuth and property-structure correlations in bismuth borate glasses, Phys. Chem. Chem. Phys. 23 (2021) 10006–10020, https://doi.org/10.1039/d1cp00301a.
[53] G. Poirier, M. Poulain, Y. Messaddeq, S.J.L. Ribeiro, New tungstate fluorophosphate glasses, J. Non. Cryst. Solids 351 (2005) 293–298, https://doi.org/10.1016/j.jnoncrysol.2004.11.017.
[54] G. Poirier, F.C. Cassanjes, Y. Messaddeq, S.J.L. Ribeiro, A. Michalowicz, M. Poulain, Local order around tungsten atoms in tungstate fluorophosphate glasses by X-ray absorption spectroscopy, J. Non. Cryst. Solids 351 (2005) 3644–3648, https://doi.org/10.1016/j.jnoncrysol.2005.08.038.
[55] E.I. Kamitsos, A.P. Patsis, G.D. Chryssikos, Infrared reflectance investigation of alkali diborate glasses, J. Non. Cryst. Solids 152 (1993) 246–257, https://doi.org/10.1016/0022-3093(93)90258-Y.
[56] J.F. Stebbins, P. Zhao, S. Kroeker, Non-bridging oxygens in borate glasses: characterization by 11B and 17O MAS and 3QMAS NMR, Solid State Nucl. Magn. Reson. 16 (2000) 9–19, https://doi.org/10.1016/S0926-2040(00)00050-3.
[57] T. Yamashita, Y. Ohishi, Concentration and temperature effects on the spectroscopic properties of Tb3+ doped borosilicate glasses, J. Appl. Phys. (2007) 102, https://doi.org/10.1063/1.2821789.
[58] M. Kumar, A.S. Rao, Influence of Tb3+ ions concentration and temperature on lithium bismuth alumino borosilicate glasses for green photonic device applications, Opt. Mater. 120 (2021) 111439, https://doi.org/10.1016/J.OPTMAT.2021.111439.
[59] T.A. Lodi, J.F.M. dos Santos, G. Galleani, L.G. Jacobsohn, T. Catunda, A.S.S. de Camargo, Promising Tb^{3+}-doped gallium tungsten-phosphate glass scintillator: spectroscopy, energy transfer and UV/X-ray sensing, J. Alloys Compd. 904 (2022) 164016, https://doi.org/10.1016/j.jallcom.2022.164016.
[60] P.S. Peijzel, A. Meijerink, R.T. Wegh, M.F. Reid, G.W. Burdick, A complete 4fn energy level diagram for all trivalent lanthanide ions, J. Solid State Chem. 178 (2005) 448–453, https://doi.org/10.1016/J.JSSC.2004.07.046.
[61] W.T. Carnall, P.R. Fields, K. Rajnak, Electronic energy levels of the trivalent lanthanide aquo ions, III. Tb^{3+}, J. Chem. Phys. 49 (1968) 4447–4449, https://doi.org/10.1063/1.1669895.
[62] M. Yamane, Y. Asahara, Glasses For Photonics, Cambridge University Press, Cambridge, 2000, https://doi.org/10.1017/CBO9780511541308.
[63] H. Becquerel, Comptes Rendus 125 (1897) 679.
[64] J.H. Van Vleck, M.H. Hebb, On the paramagnetic rotation of tysonite, Phys. Rev. 46 (1934) 17–32, https://doi.org/10.1103/PhysRev.46.17.
[65] N.F. Borrelli, Faraday rotation in glasses, J. Chem. Phys. 41 (1964) 3289–3293, https://doi.org/10.1063/1.1725727.
[66] M. Valeanu, M. Sofronie, A.C. Galca, F. Tolea, M. Elisa, B. Sava, L. Boroica, V. Kuncser, The relationship between magnetism and magneto-optical effects in rare earth doped aluminophosphate glasses, J. Phys. D (2016) 49, https://doi.org/10.1088/0022-3727/49/7/075001.
[67] G.A. Bain, J.F. Berry, Diamagnetic corrections and Pascal's constants, J. Chem. Educ. 85 (2008) 532–536, https://doi.org/10.1021/ed085p532.
[68] M. Capitelli, G. Colonna, A. D'Angola, Fundamental Aspects of Plasma Chemical Physics, 1st ed., Springer, New York, NY, 2012 https://doi.org/10.1007/978-1-4419-8182-0.
[69] J.H. van Vleck, The Theory of Electric and Magnetic Susceptibilities, Oxford University Press, New York, NY, USA, 1932. ISBN 10: 0198512430.
[70] Y.B. Saddeek, R. El Mallawany, I.S. Yahia, W. Dobrowolski, L. Kilanski, A. Avdonin, M. Arciszewska, Magnetic properties of some tellurite glasses, J. Supercond. Nov. Magn. 31 (2018) 3079–3084, https://doi.org/10.1007/s10948-018-4812-7.
[71] L. Pavić, M.P.F. Graca, Ž. Skoko, A. Moguš-Milanković, M.A. Valente, Magnetic properties of iron phosphate glass and glass-ceramics, J. Am. Ceram. Soc. 97 (2014) 2517–2524, https://doi.org/10.1111/jace.12951.
[72] H. Akamatsu, K. Fujita, S. Murai, K. Tanaka, Magneto-optical properties of transparent divalent iron phosphate glasses, Appl. Phys. Lett. 92 (2008) 3–6, https://doi.org/10.1063/1.2952460.
[73] H. Akamatsu, J. Kawabata, K. Fujita, S. Murai, K. Tanaka, Magnetic properties of oxide glasses containing iron and rare-earth ions, Phys. Rev. B 84 (2011) 1–8, https://doi.org/10.1103/PhysRevB.84.144408.
[74] R.A. Verhelst, R.W. Kline, A.M. de Graaf, H.O. Hooper, Magnetic properties of cobalt and manganese aluminosilicate glasses, Phys. Rev. B. 11 (1975) 4427–4435.
[75] M. Elisa, R. Stefan, I.C. Vasiliu, M.I. Rusu, B.A. Sava, L. Boroica, M. Sofronie, V. Kuncser, A.C. Galca, A. Beldiceanu, A. Volceanov, M. Eftimie, Thermal, structural, magnetic and magneto-optical properties of dysprosium-doped phosphate glass, J. Non. Cryst. Solids 521 (2019) 119545, https://doi.org/10.1016/j.jnoncrysol.2019.119545.
[76] F. Suzuki, T. Honma, Y. Doi, Y. Hinatsu, T. Komatsu, Magnetic properties and homogeneous distribution of Gd 3+ ions in gadolinium molybdenum borate glass with high Gd_2O_3 content, Mater. Res. Bull. 47 (2012) 3403–3406, https://doi.org/10.1016/j.materresbull.2012.07.015.
[77] K.J. Carothers, R.A. Norwood, J. Pyun, High Verdet constant materials for magneto-optical Faraday rotation: a review, Chem. Mater. 34 (2022) 2531–2544, https://doi.org/10.1021/acs.chemmater.2c00158.
[78] C.B. Rubinstein, L.G. Van Uitert, W.H. Grodkiewicz, Magneto-optical properties of rare earth (III) aluminum garnets, J. Appl. Phys. 35 (1964) 3069–3070, https://doi.org/10.1063/1.1713182.
[79] M.J. Weber, R. Morgret, S.Y. Leung, J.A. Griffin, D. Gabbe, A. Linz, Magneto-optical properties of KTb3F10 and LiTbF 4 crystals, J. Appl. Phys. 49 (1978) 3464–3469, https://doi.org/10.1063/1.325255.
[80] J. Qiu, K. Tanaka, N. Sugimoto, K. Hirao, Faraday effect in Tb3+-containing borate, fluoride and fluorophosphate glasses, J. Non. Cryst. Solids 213–214 (1997) 193–198, https://doi.org/10.1016/S0022-3093(97)00101-4.
[81] B. Bellanger, L. Audebert, Y. Ledemi, Y. Messaddeq, Superexchange interaction influence on the Faraday effect in terbium fluorophosphate glasses by co-doping with praseodymium, dysprosium, and holmium, J. Phys. Chem. C. 125 (2021) 17482–17492, https://doi.org/10.1021/acs.jpcc.1c04713.
[82] M.W. Shafer, J.C. Suits, Preparation and Faraday rotation of divalent europium glasses, J. Am. Ceram. Soc. 49 (1966) 261–264, https://doi.org/10.1111/j.1151-2916.1966.tb13253.x.
[83] M. Daybell, W.C. Overton, H.L. Laquer, The Faraday effect at low temperatures in terbium alumina silicate glass, Appl. Phys. Lett. 11 (1967) 79–81, https://doi.org/10.1063/1.1755044.
[84] Y. Zhang, S. Murai, A. Maeno, H. Kaji, M. Shimizu, Y. Shimotsuma, Z. Ma, J. Qiu, K. Tanaka, Microstructure and Faraday effect of Tb_2O_3-Al_2O_3-SiO_2-B_2O_3 glasses for fiber-based magneto-optical applications, J. Am. Ceram. Soc. 105 (2022) 1198–1209, https://doi.org/10.1111/jace.18163.
[85] K. Tanaka, K. Hirao, N. Soga, Large Verdet constant of $30Tb_2O_370B_2O_3$ glass, Jpn. J. Appl. Phys. 34 (1995) 4825–4826, https://doi.org/10.1143/JJAP.34.4825.

[86] C.B. Rubinstein, S.B. Berger, L.G. Van Uitert, W.A. Bonner, Faraday rotation of rare-earth (III) borate glasses, J. Appl. Phys. 35 (1964) 2338–2340, https://doi.org/10.1063/1.1702860.

[87] S.H. Yuan, X.Z. Shu, A new Faraday rotation glass with a large Verdet constant, J. Appl. Phys. 75 (1994) 6375–6377, https://doi.org/10.1063/1.355354.

[88] Y. Ding, K. Tanaka, L. Wondraczek, Mechanical manipulation of a fiber-optical microprobe fabricated from oxide glasses with magnetic force response, Adv. Photonics Res. 2 (2021) 2000100, https://doi.org/10.1002/adpr.202000100.

[89] M.A. Butler, E.L. Venturini, High frequency Faraday rotation in FR-5 glass, Appl. Opt. 26 (1987) 1581, https://doi.org/10.1364/ao.26.001581.

[90] V.I. Savinkov, V.N. Sigaev, N.V. Golubev, P.D. Sarkisov, A.V. Masalov, A. P. Sergeev, Borogermanate glasses with a high terbium oxide content, J. Non. Cryst. Solids 356 (2010) 1655–1659, https://doi.org/10.1016/j.jnoncrysol.2010.06.011.

[91] G. Gao, A. Winterstein-Beckmann, O. Surzhenko, C. Dubs, J. Dellith, M.A. Schmidt, L. Wondraczek, Faraday rotation and photoluminescence in heavily Tb3+-doped GeO_2-B_2O_3-Al_2O_3-Ga_2O_3 glasses for fiber-integrated magneto-optics, Sci. Rep. 5 (2015) 1–6, https://doi.org/10.1038/srep08942.

[92] H. Lin, B. Liu, L. Zhou, H. Yang, J. He, T. Zhang, H. Liu, X. Jiang, C. Li, S. Li, L. Liu, F. Zeng, Z. Su, Enhancements of magneto-optical properties of GeO_2-PbO-B_2O_3–SiO_2–P_2O_5 glass doped Tb3+ ion, Mater. Chem. Phys. (2022) 282, https://doi.org/10.1016/j.matchemphys.2022.125963.

[93] H. Guo, Y. Wang, Y. Gong, H. Yin, Z. Mo, Y. Tang, L. Chi, Optical band gap and photoluminescence in heavily Tb3+ doped GeO_2-B_2O_3-SiO_2-Ga_2O_3 magneto-optical glasses, J. Alloys Compd. 686 (2016) 635–640, https://doi.org/10.1016/j.jallcom.2016.06.074.

[94] Z.X. Mo, H.W. Guo, P. Liu, Y.D. Shen, D.N. Gao, Luminescence properties of magneto-optical glasses containing Tb3+ ions, J. Alloys Compd. 658 (2016) 967–972, https://doi.org/10.1016/j.jallcom.2015.10.236.